Experiments and simulations of the ballistic response of ceramic composite armors

Jinfeng Cao, Jianzhong Lai, Jiehang Zhou, Ningyu Kang, Longyu Du and Yiqiu Miao

School of Materials Science and Engineering, Nanjing University of Science and Technology, Nanjing 210094, China

Abstract   A lightweight multilayer ceramic composite armor with a sandwich structure back plate was proposed by studying the penetration process, damage mechanism, and the function of each layer of the composite armor against the 12.7 mm armor-piercing projectile. The effectiveness of the simulation was verified by comparing the experimental and simulation data. The effects of crack initiation in the ceramics, abrasion of ceramics, and size of ceramic cones on the penetration resistance of targets were discussed. The structural configuration of backplate sequence and thickness ratio was optimized through finite element simulation on ANSYS/LS-DYNA. Results indicate that boundary constraints have a significant effect on the antipenetration performance of ceramics. The antipenetration performance is the best when the structure of restrained composite armor is Al6061/Al_2O_3/TC4/ Kevlar$^®$/TC4 and the thickness ratio of the TC4 transition and back plates is 4:3.

1. Introduction

Armor protection technology is being developed toward the direction of homogenous weight, rough preparation, single function to high functionality, lightweight compounding, and intelligentization [1]. Radin et al. [2] found that layered structures in contact provide better results than monolithic structures with the same total weight. Ali et al. [3] studied the projectile penetration in a multilayered armor consisting of a perforated steel plate and an aluminum base armor. Armored steel, aluminum alloys, titanium alloys, ceramics, and fiber/resin matrix composites constitute a modern armor protection material system after long-term research and practice [4-6]. Ong et al. [7] proposed a concept of layered armor sequence. The results showed that ceramics cannot serve as a good panel without the second layer because of their brittle fracture behavior. Hu et al. [8] tested a 7.62 mm projectile-penetrating SiC/ultra-high-molecular-weight polyethylene (UHMWPE) composite armor. The penetration process was divided into four stages to study the function of each layer.

The design of back plate is important to avoid the premature destruction of ceramic panel. Goh et al. [9] studied the effects of steel hardness on ceramic armor against long rod impact. The results showed that the panel hardness has minimal effect on the antipenetration performance of the armor structure, and the increase in back plate hardness is beneficial. Wang et al. [10] used the composite laminate of Ti6Al4V/UHMWPE/Ti6Al4V as back plate materials because of the high strength and tenacity of Ti6Al4V. Kolopp et al. [11] compared sandwich structures subjected to medium-velocity impacts to determine the roles of each part and possible couplings.

Each layer's thickness parameter affects the antipenetration performance after selecting the armor material and determining the basic structure of the target.

Hetherington et al. [12] conducted ballistic impact tests of ceramic/aluminum composite armor under certain areal density. The results showed that an optimal thickness ratio is found in the configuration. Lee et al. [13] studied the optimal value of thickness ratio and indicated that

the optimal value for two-layer configurations is 2.5.

Finite element method (FEM) is a reasonable and efficient method used for penetration research. Cortés et al. [14] conducted numerical simulation to simulate the penetration process of ceramic/aluminum composite armor. Li et al. [15] performed depth of penetration tests and numerical simulations to investigate the ballistic performance of alumina ceramic/603 steel composite targets against projectiles. Bürger et al. [16] presented a numerical model for ballistic impact simulations in hybrid ceramic/fiber-reinforced composite armors. Shi et al. [17] discussed the effects of constraints on the optimal thickness and ballistic performance and found that the double-constrained optimization problem can be simplified. Lee et al. [13] used smoothed particle hydrodynamics to simulate the penetration process of the projectile impacting a ceramic/metal target and found that the effects of thickness ratio on the anti-penetration performance are obtained with a given areal density. Holland et al. [18] conducted a design study of steel-alumina targets through finite element simulations. The results showed that the metal/ceramic structure has the highest ballistic performance.

In this study, a ceramic/fiber/metal armor called "sandwich" structure was proposed, and a transition layer between the ceramic panel and the fiber plate was added to improve the performance of back plate. ANSYS/LS-DYNA was used to simulate the penetration process against the 12.7 mm armor-piercing (AP) projectile. The coupling relationship between the metal/ceramic/fiber composite structures by comparing the experimental and simulation results was investigated to achieve a suitable design of structural configuration.

2. Experiment

2.1 Ballistic test conditions and damage judgement

As shown in Fig. 1, a projectile propelling mechanism was used to launch the 12.7 mm AP projectile. The schematic of the ballistic test, including the bullet, tinfoil target velocimeter, composite targets, and supporting pedestal, is shown in Fig. 1. The mass, diameter, length, volume, and density of the projectile core are 16.8 g, 10.9 mm, 31.8 mm, 2260.5 mm^3, and 7.43 g/cm^3, respectively. The launcher's level was maintained by adjusting the assembly device. The tinfoil targets were used to calculate the bullet's velocity by recording the time when a bullet passes through two tinfoil targets. The projectile velocity ranges from 817 m/s to 825 m/s in all tests.

The experimental results were compared with the damage rating standards in Table 1. In addition, a protective factor N was used to evaluate the comprehensive anti-penetration performance of the armor, which can be expressed as

$$N = (\rho_A \times h_A) / (\rho_B \times h_B),\qquad(1)$$

where ρ_A and h_A are the density and thickness of rolling

Table 1. Damage rating standard.

| Damage rating	Damage description
Grade 1	A slight damage crater on the front and no bulge at the back
Grade 2	An arbitrary shape crater on the front and a bulge at the back
Grade 3	A deep crater on the front and an uncracked bulge with white pattern at the back
Grade 4	A deep crater on the front and a cracked bulge with kerosene impermeability at the back
Grade 5	Kerosene-permeable crack at the back
Grade 6	Ring rip or obvious plug at the back
Grade 7	Bullet stuck or backside collapse
Grade 8	Perforation
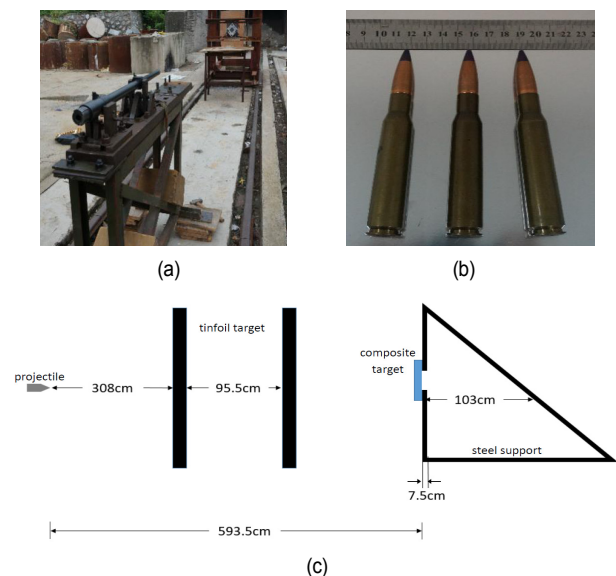
Fig. 1. Sites and equipment of the penetration experiment: (a) Ballistic gun; (b) AP projectile; (c) schematic of the ballistic test.
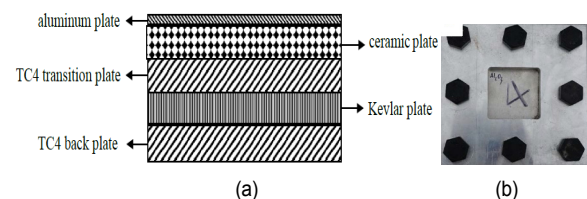

Fig. 2. Composite target and constraint fixture: (a) Structure of composite armor; (b) target A-4 and constraint fixture.

homogenized armored steel, respectively, and ρ_B and h_B are the density and thickness of armored material to be examined, respectively.

2.2 Materials and targets

A lightweight multilayer composite armor with a sandwich backplate was designed. As shown in Fig. 2(a), the components of the composite target from the strike surface to the

Table 2. Structural configuration of group A.

Group number	T_{Al} (mm)	$T_{ceramic}$ (mm)	T_{TC4} (mm)	T_{Kevlar} (mm)	T_{TC4} (mm)	Areal density (g/cm²)	Thickness ratio A
A-1	1	14	4	5	3	9.93	4:3
A-2	1	14	2	5	5	9.93	2:5
A-3	1	14	4	5	3	9.93	4:3
A-4	1	14×2	4	5	3	15.62	4:3

Notes: T_{Al}, $T_{ceramic}$, T_{TC4}, T_{Kevlar}, and T_{TC4} denote the thickness of 6061 aluminum alloy, Al_2O_3 ceramics, TC4 transition plates, Kevlar fiber, and TC4 back plates, respectively.

back surface were 6061 aluminum alloy, Al_2O_3 ceramic/TC4 titanium alloy, Kevlar® fiber, and TC4 titanium alloy. First, two layers of TC4 and Kevlar® plates were bonded together using epoxy resin AB glue. Second, the Al_2O_3 panel was coated with 704 silica binder and bonded with the sandwich backplate. Finally, the 6061 aluminum alloy skin was bonded to the target with epoxy resin AB glue.

The performance of ceramics was related to their constraints. As shown in Fig. 2(b), the aluminum alloy fixture was designed for circumferential restraint. Group A targets were prepared to make a comparative study in this section. A-1 and A-2 were unconstrained with different backplane configurations. A-1 and A-3 had the same components but the latter was constrained. A-4 had double-layer ceramics. The length and width of all targets were 100 mm. The structural configuration of the targets is shown in Table 2.

3. Numerical simulation

3.1 Numerical models and contact definitions

ANSYS/LS-DYNA was used to construct a simulation model for studying the damage mechanism of ceramic panel and the effects of back laminates. The projectile geometry is simplified with a dimension of Ø10.9 mm × 31.8 mm and an initial incident velocity of 820 m/s. The curvature radius of the projectile head was 28.62, mm and the material of the projectile was steel 4340, as shown in Fig. 3(a). One-fourth of the model was used to improve the computing inefficiency caused by the axisymmetric nature of the problem. The contact between the projectile and multilayers was defined on the basis of eroding surface to surface. The connection between adjacent layers was defined using a contact algorithm called automatic surface-to-surface tiebreak. The symmetry plane applied displacement constraints in the x and y directions, and the perimeter of the target was fully constrained. The simulation model of the composite target is shown in Fig. 3(b).

The configuration changes were adjusted in accordance with the experiment, and the relevant material properties and boundary condition settings remained unchanged. The simulation will be immediately terminated, and the required simulation results cannot be obtained when the calculation in ANSYS/LS-DYNA fails to converge. In this study, the convergence of the
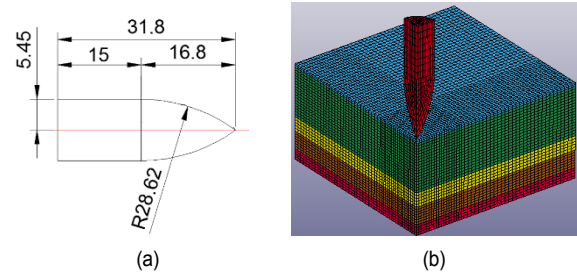

Fig. 3. Simulation model of the projectile and the composite armor: (a) Projectile size (mm); (b) simulation model.

simulation was controlled by defining the suitable contact, matching mesh size, correct model parameters, and mass and energy conservation control.

3.2 Numerical models and contact definitions

The Johnson-Cook (J-C) model (Mat_15), which is suitable for large strain rates, was used to describe the dynamic mechanical behavior of steel 4340, TC4, and Al6061 [19]. The flow stress in this model is expressed as:

$$\sigma = [A + B\varepsilon_p^n][1 + C\ln\dot{\varepsilon}^*][1 - (T^*)^m] . \qquad (2)$$

The J-C damage model is expressed as [19]:

$$D = \Sigma(\frac{\Delta\varepsilon_p}{\varepsilon_p^f}), \qquad (3)$$

where D is the damage parameter, and ε_p^f is the effective failure strain given by [20]:

$$\varepsilon_p^f = \left[D_1 + D_2\exp(D_3\sigma^*)\right]\left[1 + D_4\ln\dot{\varepsilon}^*\right]\left[1 + D_5T^*\right] . \qquad (4)$$

A detailed description on the model formulation can be found in Refs. [19, 21]. The J-C model constants are listed in Table 3 [20-25].

Johnson-Holmquist (JH-2) ceramic model (Mat_110) [26-31] was adopted to simulate the brittle behavior of Al_2O_3) ceramic. The associated parameters of alumina ceramic in the JH-2 model are given in Table 4 [23-25]. The normalized equivalent stress in the JH-2 model is expressed as:

$$\sigma^* = \sigma_i^* - D(\sigma_i^* - \sigma_f^*) . \qquad (5)$$

The stresses became dimensionless through normalization to the equivalent stress at the Hugoniot elastic limit (HEL), which can be expressed as:

$$\sigma^* = \sigma / \sigma_{HEL} . \qquad (6)$$

The normalized intact and fracture strengths are expressed as:

Table 3. J-C model parameters of steel 4340 [20, 22, 23], TC4 [23], and Al6061 [21, 24].

Parameters	ρ (kg/m^3)	G (GPa)	A (GPa)	B (GPa)	n	c	m	T_m (K)	T_r (K)
Steel 4340	7850	77	0.792	0.51	0.26	0.014	1.03	1793	294
TC4	4450	41.9	1.098	1.092	0.93	0.014	1.1	1878	294
Al6061-T6	2705	27.6	0.335	0.085	0.11	0.012	1.0	875	294
Parameters	Cp	D1	D2	D3	D4	D5	C (m/s)	S1	γ_0
Steel 4340	477	0.05	3.44	−2.12	0.002	0.61	4569	1.49	2.17
TC4	560	−0.09	0.27	0.48	0.014	3.87	5130	1.028	1.23
Al6061-T6	963	0.096	0.049	−3.46	0.016	1.09	5240	1.4	1.97

Table 4. JH-2 model parameters of Al$_2$O$_3$ ceramic [23-25].

Parameters	ρ (kg/m^3)	G (GPa)	A (GPa)	B (GPa)	c	m	n	epsi	T
Al$_2$O$_3$	3850	152	0.989	0.77	0.0045	1.0	0.375	1.0	0.26
Parameters	HEL	Phel	$D1$	$D2$	FS	$K1$ (GPa)	$K2$ (GPa)	K3 (GPa)	
Al$_2$O$_3$	6.57	3.6	0.005	1.0	1.0	184.56	185.87	157.54	

Table 5. Ortho model parameters of Kevlar [32].

Parameters	ρ (kg/m^3)	EA (GPa)	EB (GPa)	EC (GPa)	PRBA	PRCA	PRCB	GAB (GPa)
Kevlar	1440	35	35	8.33	0.0045	0.044	0.044	0.35
Parameters	GBC (GPa)	GCA (GPa)	Alph	Kfail (GPa)	Aopt	Macf	Sc (GPa)	Xt (GPa)
Kevlar	0.32	0.32	0	2.2	1.0	3	0.025	0.725
Parameters	Yt (GPa)	Yc (GPa)	Sn (GPa)	Syz (GPa)	Szx (GPa)	-	-	-
Kevlar	0.725	0.69	9.0	1.08	1.8	-	-	-

$$\sigma_i^* = A(P^* + T^*)^N [1 + C\ln(\dot{\varepsilon} / \dot{\varepsilon}_0)] , \qquad (7)$$

$$\sigma_f^* = B(P^*)^M [1 + C\ln(\dot{\varepsilon} / \dot{\varepsilon}_0)] , \qquad (8)$$

where A, B, C, M, and N are material constants, and D is the damage factor ($0 \le D \le 1$).

The damage is assumed to accumulate through incremental plastic deformation ε_p:

$$\varepsilon_p^f = D_1 (P^* + T^*) D_2 . \qquad (9)$$

The pressure model is expressed as:

$$P = K_1 \mu + K_2 \mu^2 + K_3 \mu^3 + \Delta P , \qquad (10)$$

where K_1, K_2, K_3 are constants, and μ is the compressibility factor.

The Kevlar fiber is modeled using the composite damage (Mat_22) model. A set of orthotropic constitutive relations was used to define the relationship between stress and strain. The failure modes defined by Mat add erosion were divided into
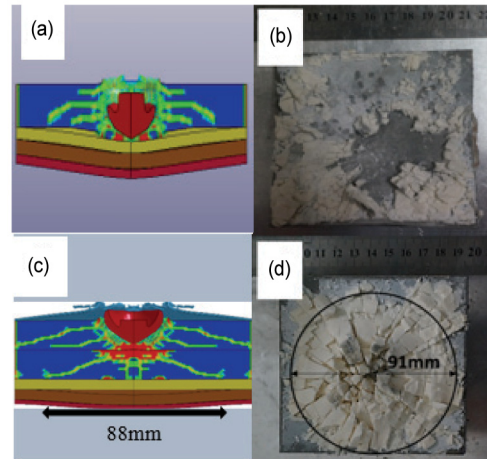

Fig. 4. Ceramic damage: (a) Simulation results of A-3; (b) experiment results of A-3; (c) simulation results of A-4; (d) experiment results of A-4.

four categories, namely, tensile failure of fibers, compressive failure of fibers, tensile failure of matrix, and compressive failure of matrix. A detailed description can be found in Ref. [32], and the associated material parameters are listed in Table 5 [32].

3.3 Validation of numerical models

To verify the validity of the finite element model, the damage of ceramic plates and the deformation of the back plates of A-3 and A-4 targets were compared through experiment and simulation. The ballistic limit of A-3 target was simulated and compared with the result of the formula.

The crack in the ceramic plate that propagated to the edge is shown in Fig. 4(a). A large area of the ceramic was separated from the metal surface, and the residual fragments were broken into small pieces, which are consistent with the experimental result of A-3, as shown in Fig. 4(b). The first layer of Al$_2$O$_3$ ceramics was severely broken, and the second layer showed an evident ceramic cone of A-4. Small fragments with the shape of a ceramic cone appeared near the impact point in the staircase extension, as shown in Figs. 4(c) and (d) which is consistent with the experimental result. The simulated and experimental diameters and heights of the ceramic cone were 88 and 13 mm and 91 and 12 mm, respectively. The overall error was approximately 5 % which was mainly caused by the simplification of the simulation model and the breaking loss in the experiments.

The simulation and experiment results of A-3 metal and Kevlar plate are shown in Fig. 5. The uplift of TC4 transition plate was 8.4 mm, and the experimental result was 10.2 mm. The uplift of TC4 back plate was 7.5 mm, and the experimental result was 7.8 mm. The two were basically consistent. The main reason for the deformation errors was the slight differences in material performance between the numerical simulation and actual experiments.

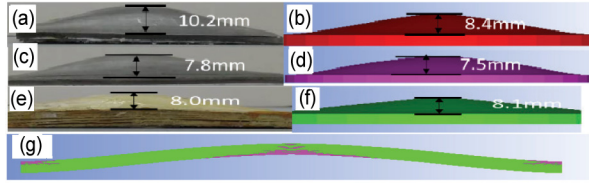The uplift of Kevlar® plate was 8.1 mm, and the experimental

Fig. 5. Backplane deformation: (a) Experiment results of transition plate; (b) simulation results of transition plate; (c) experimental results of back plate; (d) simulation results of back plate; (e) experimental results of Kevlar plate; (f) simulation results of Kevlar plate; (g) 2D interface diagram.

result was 8.0 mm, which was consistent with each other. The Kevlar® plate was laminated with multilayer fiber cloth. Stratification occurred under the combined action of stress and reflection waves [33]. Stratification was observed in the 2D diagram, which was consistent with the simulation result. The existing error was mainly because of the model simplification.

In accordance with the law of conservation of energy and momentum, a simplified theoretical model was established using an integral method. Bethe and Taylor assumed that the motion equation of the projectile penetrating the target with H thickness is expressed by equivalent resistance stress σ_r:

$$F = M\frac{dV}{dt} = MV\frac{dV}{dx} = \sigma_r = \text{constant} , \tag{11}$$

where M and R are the mass and radius of the projectile, respectively. Using the boundary condition, $V_0 = V_{bl}$ when $x = 0$, whereas $V_0 = 0$ when $x = H$. Integrating the above equation yields:

$$\frac{MV_{bl}^2}{2} = \pi \cdot r^2 H\sigma_r . \tag{12}$$

Substituting $M = \rho_P \pi r^2 L_{eff}$, where L_{eff} is the equivalent length of projectile, and ρ_P is the projectile density, we have:

$$V_{bl} = \sqrt{\frac{2H\sigma_r}{\rho_p L_{e_{ff}}}} . \tag{13}$$

D is the diameter of the projectile:

$$\frac{\sigma_r}{Y_t} = 2/3 + 4\frac{H}{D} , \quad \frac{H}{D} \leq \frac{1}{3} , \tag{14}$$

$$\frac{\sigma_r}{Y_t} = 2 , \quad \frac{1}{3} \leq \frac{H}{D} \leq 1.0 , \tag{15}$$

$$\frac{\sigma_r}{Y_t} = 2.0 + 0.8\ln\left(\frac{H}{D}\right), \quad \frac{H}{D} \geq 1 . \tag{16}$$

The law of conservation of energy states that:

$$\frac{1}{2}MV_0^2 = \frac{1}{2}MV_r^2 + W_p , \tag{17}$$

Table 6. Ballistic limit velocity V_{bl}.

Group number	Initial velocity V_0 (m/s)	Simulation result	Theoretical value V_{bl} (m/s)
A-3-V920	920	Y	
A-3-V871	871	N	
A-3-V895	895	N	942
A-3-V913	913	Y	
A-3-V910	910	N	
A-3-V911	911	Y	

Notes: Y represents complete penetration, and N represents no penetration.

where v_0 and v_r are the initial and esidual velocities after the penetration, respectively. The ballistic limit velocity is defined as the impact velocity when $v_r = 0$:

$$\frac{1}{2}MV_{bl}^2 = W_p . \tag{18}$$

Substituting Eq. (15) into Eq. (14) yields:

$$V_0^2 = V_r^2 + V_{bl}^2 . \tag{19}$$

Considering the composite armor structure, the residual velocity of a projectile passing through a layer is equal to the velocity of the next layer. The relative velocity equation of N-layered targets is obtained on the basis of energy conservation (Eq. (16)):

$$V_{ri}^2 = V_{0i}^2 - V_{bli}^2 , \tag{20}$$
$$V_{ri} = V_{0(i+1)} . \tag{21}$$

Accumulating all equations yields:

$$V_{bl} = \sqrt{\sum_{i=1}^{N} V_{bli}^2} . \tag{22}$$

Ballistic limit velocity V_{bl} of the 12.7 mm AP projectile vertically impacted on A-3 target calculated using Eqs. (13) and (19) was 942 m/s, as shown in Table 6. The value of V_{bl} simulated using the FEM was 910 m/s. In the table, Y indicates complete penetration, and N indicates no penetration.

The geometric model, material parameters, control parameters, and boundary conditions are consistent with the experimental results, and can be used for the next optimal design of antipenetration numerical simulation.

4. Results and discussion

4.1 Ballistic experiment analysis

Protective coefficient N for A-1, A-2, A-3, and A-4 calculated using Eq. (1) were 2.49, 2.49, 2.49, and 1.61, respectively. The
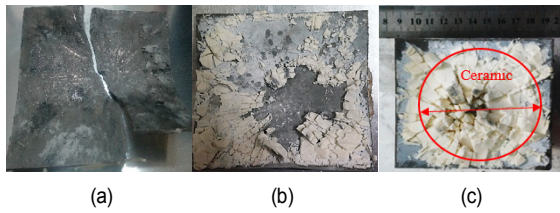
Fig. 6. TC4 transition plate damage: (a) A-1; (b) A-3; (c) A-4.

A-3 armor was compliant with the grade 1 damage, and the A-4 armor was compliant with the grade 2 damage in Table 1, making them as qualified armor. Whether constrained or not has a great influence on the antipenetration performance of the target. The A-1 and A-2 targets, whichwere unconstrained, were seriously damaged, and the target materials were difficult to collect. When the projectile penetrated the A-1 target, the TC4 transition plate was divided into two parts because no constraints were imposed, as shown in Fig. 6(a). Compared with A-1, no crack was observed in the TC4 transition plate of the constrained A-3 target, as shown in Fig. 6(b), indicating that the metal deformation was within the plastic range and no failure occurred. On the one hand, the back plate support function cannot be properly executed without constraint, thereby leading to premature ceramic fracture. On the other hand, the ceramic fragments and the projectile were insufficiently abraded without constraint. The projectile penetrated the back plate in advance and failed to utilize the performance of ceramics. Therefore, boundary constraints have a significant influence on the antipenetration performance of ceramics.

The function of the TC4 transition plate is to provide high strength support for the ceramic layer and increase ceramic abrasion. The Kevlar plate serves as a buffer balance in the entire backplane composite structure. The TC4 back plate directly affects the energy balance of the middle layer. A gap was found between the Kevlar and TC4 back plates after the penetration, as shown in Fig. 4(a), and delamination occurred between the fiberboards of the Kevlar board. On the basis of the calculation of reflection wave [33], the interface of Kevlar and TC4 back plates was a tension wave, making it easy to separate. Increasing a new stress buffer layer between the Kevlar and TC4 back plates and the bonding force at the interface are two optimization directions for improving the antipenetration performance of the target.

The first ceramic layer of A-4 target was crushed and cannot be collected. The second ceramic layer of A-4 target was still bonded to the backplane with complete patterns of the ceramic cone. The ceramics near the bullet point area were broken into small ceramic blocks, as shown in Fig. 6(c). The ceramic far from the bullet point area was cracked and broken into large pieces, forming a distinct ceramic cone section. The diameter and height of the ceramic cone were 91 and 12 mm, respectively. The area was 6358 mm^2, accounting for 81 % of the total area. As shown in Fig. 6(b), the ceramic layer of A-3 target collapsed but the trace of the ceramic cone remained visible. The cracks were denser and smaller than those of the A-4
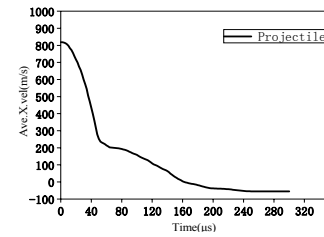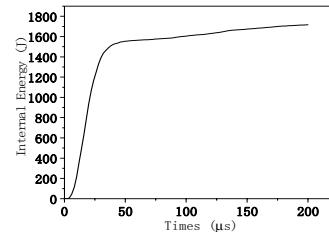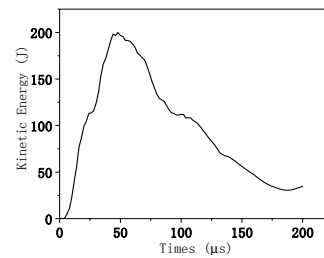
Fig. 7. Energy histories of the A-3 target: (a) Projectile residual velocity; (b) kinetic energy histories of the ceramic layer; (c) eroded internal energy histories of the ceramic layer.

target. First, the A-4 target had two layers of ceramic plates. The first layer collapsed and absorbed a large amount of energy. The velocity of the projectile was lower than the initial velocity when the second layer was penetrated. The energy of the projectile was small, and the second layer absorbed a small amount of energy. Second, the two ceramic layers increased the penetration process against the thickness and obstructed the expansion of ceramic cracks. This finding indicated that the microcracks in the second layer of ceramics should be reactivated. Finally, the energy absorbed by the ceramics mainly came from ceramic fractures. Many ceramic cracks can be induced when the kinetic energy of the bullet was large. The ceramics broke into small pieces or powders, thereby increasing their absorbed energy. Appropriately increasing the thickness, requiring the crack to regenerate in the ceramic plate, and thorough ceramic crushing are the three optimized design directions to improve the antipenetration performance of the target.

4.2 Impact simulation analysis

The penetration process was divided into four phases in accordance with the velocity curve of the projectile and the damage of the target, as shown in Figs. 7-9.
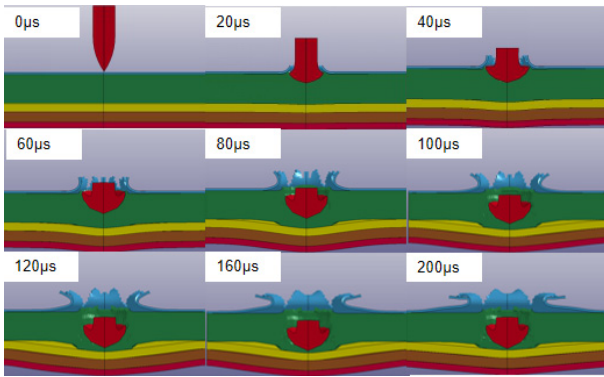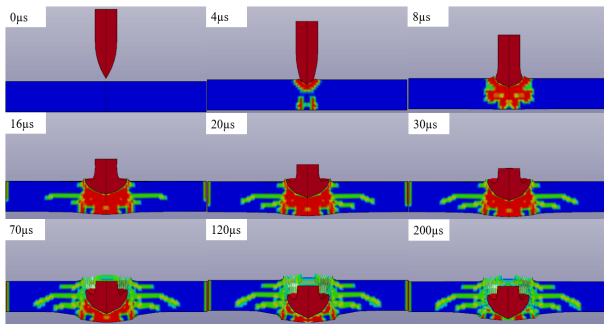
Fig. 8. Simulation of the penetration process (0-200 μs).

Fig. 9. Damage distribution diagram of the penetration process (0-200 μs) of A-3 ceramic panel.

In the first phase (no-load phase), $t < 2$ μs, and the projectile did not touch the ceramic panel, as shown in Fig. 8. In the second phase (hard collision phase), 2 μs $\leq t \leq 45$ μs, and the projectile began to penetrate the ceramic panel. The velocity sharply decreased to 434 m/s. The projectile acted on the high-hardness ceramic panel along with the upsetting and breakage of the projectile. The backplane was slightly deformed but remained in the elastic range. The projectile and the target were in a hard collision phase, and the strength of the material played the largest role. In the third phase (abrasion phase), 45 μs $\leq t \leq 160$ μs, and the projectile penetrated the ceramic and began to act on the TC4 transition plate when $t = 160$ μs, as shown in Fig. 9. The velocity decreased to 10 m/s but did not exhibit abrupt changes compared with the second phase, as shown in Fig. 7(a). The ceramics broke into pieces. The projectile's movement was blocked by its abrasive action with ceramic fragments rather than the strength. In the fourth phase (backplane penetration phase), 160 μs $\leq t \leq 200$ μs, the projectile directly acted on the backplane, and the velocity decreased to zero. The large deformation of the Kevlar® plate increased the force area and weakened the impact acting on the TC4 back plate. The acoustic impedance ratio of the Kevlar®/TC4 interface was 0.42, and the reflected wave R was negative [34]. This finding indicated that the reflected wave was a tensile wave leading to the delamination phenomenon between Kevlar® and TC4. Therefore, the bonding force between TC4/Kev-
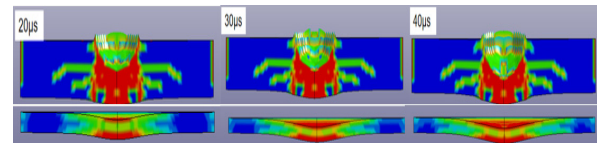

Fig. 10. Relationship between the size of ceramic cone and the stress of A-3 TC4 transition plate.

lar®/TC4 should be strengthened.

Figs. 7(b) and (c) show the energy histories of the ceramic layer. The kinetic energy of the ceramic plate reached its peak near 45 μs, and the change in the internal energy of the ceramic plate reduced. This condition was because the internal energy of the ceramic plate changed from the fracture energy of broken ceramic to the internal energy consumed by abrasion, which is called eroded internal energy. The maximum fracture energy was observed at approximately 45 μs. The performance of the ceramic was crucial for improving the anti-penetration performance of the composite target. The anti-penetration performance can be effectively improved when the abrasion time can be increased in the remaining abrasion phase.

The ceramic breakage was mainly concentrated in the second and third phases. At 4 μs, the ceramic cone formed by the compressional and reflected waves appeared at the bottom of the ceramic panel, and the cracks near the impact point began to extend outward, as shown in Fig. 9. The ceramic cone enlarged at 8 μs $\leq t \leq 20$ μs. The ceramic crush zone was formed in the central area, and a broken zone was formed by the crack propagation in the vicinity of impact point. At 30 μs $\leq t \leq 200$ μs, the projectile intruded the interior of the ceramic and was abraded by the ceramic chip. The ceramic cone's morphology was destroyed. The cracks that spread away converged together and formed a large-scale breaking zone. The ceramic panel and the metal plate were deboned, and the ceramic fragments were pressed into the deboned area. This condition indicated that the abrasion time will be effectively prolonged and the antipenetration performance will improve when the cohesion force between the ceramic and the backplane or its strength increased.

Fig. 10 shows the von Mises stress distribution of the transition metal plate when 20 μs $\leq t \leq 40$ μs. The force of the transition plate was closely related to the formation of the ceramic cone when the bullet penetrated the ceramic. At this time, the elastic body and the ceramic fragment acted on the support plate, the force range of the transition plate was the action area of the ceramic cone, the deformation range of the transition metal plate was concentrated in the ceramic cone angle, and the stress was concentrated at the boundary of the ceramic cone. Therefore, the size of the ceramic cone in the ceramic/metal composite target can affect the stress of the back plate and the force of the discrete back plate. The stress area of the back plate can be expanded and the failure of the piercing plug caused by stress concentration can be avoided by expanding the size and area of the ceramic cone.

Table 7. Structural configuration of group B.

| Group		First layer	Second layer	Third layer	Fourth layer
B-1	Material	Al	Al₂O₃	TC4	Kevlar
	Size	100×100×1	100×100×12	100×100×7	100×100×5
B-2	Material	Al	Al₂O₃	Kevlar	TC4
	Size	100×100×1	100×100×12	100×100×5	100×100×7
B-3	Material	Al	TC4	Al₂O₃	Kevlar
	Size	100×100×1	100×100×7	100×100×12	100×100×5
B-4	Material	Al	TC4	Kevlar	Al₂O₃
	Size	100×100×1	100×100×7	100×100×5	100×100×12
B-5	Material	Al	Kevlar	Al₂O₃	TC4
	Size	100×100×1	100×100×5	100×100×12	100×100×7
B-6	Material	Al	Kevlar	TC4	Al₂O₃
	Size	100×100×1	100×100×5	100×100×7	100×100×12

Note: The unit of size is mm×mm×mm.

5. Influence of the configuration parameter of the armor structure

Few related studies are conducted on the influence of the structural configuration of multilayer composite targets. This section will discuss: 1) The influence of the sequence of armored materials on the antipenetration performance under the same materials and areal density; 2) the influence of layer thickness ratio between the TC4 transition and back plates on the antipenetration of the ceramic/metal/fiber/metal armor structure.

5.1 Influence of armored material sequence

Numerical simulation was used to analyze the influence of the Al₂O₃, TC4, and Kevlar® sequences on the antipenetration performance under the same areal density. The antipenetration performance of the target was reflected by the velocity of the remaining projectile. The target configuration was recorded as group C, as shown in Table 7. The results of the six composite armors in group C penetrated at a high velocity of 820 m/s are shown in Fig. 11.

The remaining velocities of B-5 and B-6 were 384.50 and 569.61 m/s, respectively, when Kevlar® was used as a panel. From the velocity-time curve, the velocity deceleration period of B-5 was longer than that of B-6. In other words, the Kevlar's resistance to the projectile was insufficient. The structure of Al₂O₃/TC4 was better than that of TC4/Al₂O₃, indicating that the ceramics required high-strength backplane to exert their own strength properties. The remaining velocities of B-3 and B-4 were 548.58 and 507.44 m/s, respectively, when TC4 was used as a panel. The ceramics exhibited superior performance when supported by a backplane. The projectile pierced through the target after 50 μs, as shown in Fig. 11(c). The penetration process had the shortest time and the highest remaining velocity compared with other structural configurations. The remaining velocities of B-1 and B-2 were 117.23 and 217.60 m/s,
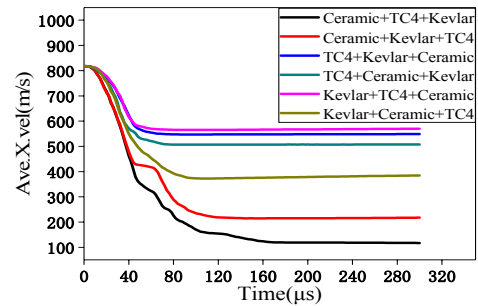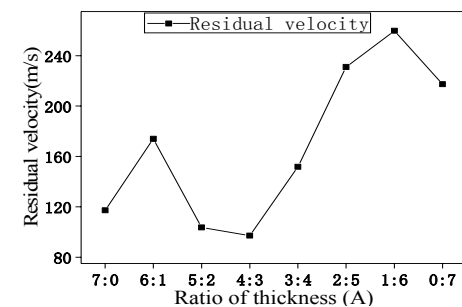

(a)
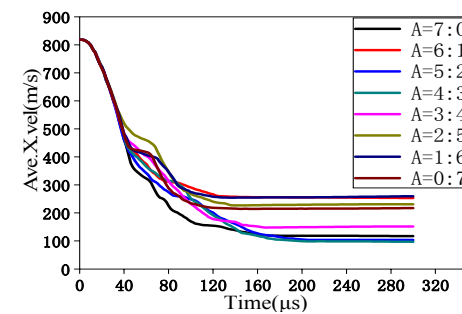
(b)
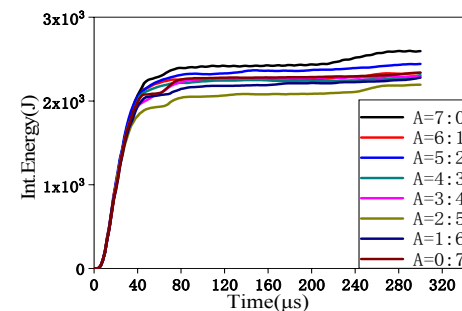
(c)

(d)

Fig. 11. Simulation results: (a) Projectile velocity of group C; (b) velocity curve of group D; (c) internal energy of the ceramics in group D; (d) relationship between the residual velocity of projectile and thickness ratio.

respectively, when ceramic was used as a panel. The acceleration of the projectile was the highest compared with other structural configurations when 0 μs ≤ t ≤ 40 μs. The deceleration phase experienced by B-1 was longer than that of B-2, and the Kevlar® backplane experienced long penetration time. This finding showed that the optimal configuration increased the

Table 8. Structural configuration of the targets.

Group number	T_{Al} (mm)	$T_{ceramic}$ (mm)	T_{TC4} (mm)	T_{Kevlar} (mm)	T_{TC4} (mm)	Areal density (g/cm^2)	Thickness ratio A
C-1	1	12	0	5	7	8.79	0:7
C-2	1	12	1	5	6	8.79	1:6
C-3	1	12	2	5	5	8.79	2:5
C-4	1	12	3	5	4	8.79	3:4
C-5	1	12	4	5	3	8.79	4:3
C-6	1	12	5	5	2	8.79	5:2
C-7	1	12	6	5	1	8.79	6:1
C-8	1	12	7	5	0	8.79	7:0

Note: T_{Al}, $T_{ceramic}$, T_{TC4}, T_{Kevlar}, and T_{TC4} denote the thickness of 6061aluminum alloy, Al$_2$O$_3$ ceramics, TC4 transition plates, Kevlar fiber, and TC4 back plates, respectively.

abrasion time.

The ceramic as the panel had the best antipenetration performance. The structure of Al$_2$O$_3$/TC4/Kevlar® (B-1) was the optimal configuration. The combination of Al$_2$O$_3$/TC4 provided the maximum acceleration at the initial phase. This condition was because breaking and preventing the projectile from penetrating forward during the initial collision is important. With the help of the high modulus and high toughness of Kevlar® fiber, the ceramics fully utilize their high elastic modulus and high hardness, thereby effectively preventing the backplane from breaking and secondary damage.

5.2 Influence of the layer thickness ratio of the target

In the numerical simulation of this section, thickness ratios A of the TC4 transition and back plates were set to 0:7, 1:6, 2:5, 3:4, 4:3, 5:2, 6:1, and 7:0. The remaining projectile velocity was used to characterize the antipenetration performance of the target. The target size was 100 mm × 100 mm, and the target configuration was Al6061/Al$_2$O$_3$/TC4/Kevlar®/TC4 (denoted as group D). The detailed experimental scheme is shown in Table 2. The influence of the thickness ratio is shown in Figs. 11(d) and (e).

No difference was found in the ceramic energy absorption between the targets with different thickness ratios in the hard collision phase. The velocity curve slowly decreased and exhibited small amplitude jitter in the abrasion phase. The roughness of the curve was caused by the abrasion. In this phase, the abrasion time of C-1, C-2, and C-3 was approximately 80 µs, and the residual velocities were more than 200 m/s. The thicknesses of TC4 transition plate were 0, 1, and 2 mm, all of which cannot provide sufficient support for the ceramic panels. This condition caused the premature failure of the transition plate and many stresses to the backplane. The abrasion time of C-4, C-5, C-6, C-7, C-8 was approximately 120 µs, and the residual velocities were less than 200 m/s. The thick TC4 transition plate provided sufficient strength to form large ceramic

cones. Large ceramic cones caused large force area of the backplane, resulting in small deflection.

As shown in Fig. 11(f), the trend of residual velocity first increased, decreased, and then increased again with the changed in the thickness ratios of C-1 to C-8. This condition was because the Kevlar® did not exert its high toughness effect when the backplane was sufficiently thick. Thus, the target can be optimized by adjusting the thickness ratio when the areal density was constant. C-5 with a thickness ratio of 4:3 was the optimal configuration.

6. Conclusions

A lightweight multilayer composite armor was proposed in this study. The processes of the 12.7 mm AP projectiles penetrating into the composite armor and the damage mechanism were investigated. The combined experimental and simulation techniques were used to explore the influence rule of the antipenetration performance of the ceramic/metal/fiber/metal structural configuration. The main results of this study are summarized as follows:

(1) A vertical impact test of 12.7 mm AP projectiles at a velocity of 820 m/s was performed on four groups of ceramic composite armors. The damage mechanism of the armor materials under each structure was compared and analyzed. The TC4 transition plate provided high strength support for the ceramic layer and increased the ceramic abrasion. The Kevlar plate served as a buffer balance in the entire backplane composite structure. The TC4 back plate directly affected the energy balance of the Kevlar layer. The boundary constraints had a significant influence on the antipenetration performance of the ceramics. The areal density was 99.3 kg/m^2, and the protection factor reached 2.49. The objectives of lightweight and high strength were realized.

(2) The damage characteristics of each layered structure were obtained, and the effectiveness of numerical simulation was verified. Numerical simulation was used to obtain the penetration process, velocity curve, energy absorption, and damage mechanism of the ceramics. The results showed that four phases of penetration, namely, no-load, hard-to-hard, abrasion, and backplane penetration phases, were found. The development and damage of the ceramic cone were analyzed. The internal cracks underwent initiation, expansion, and confluence under the combined action of shock and compression waves. The stress distribution of the transition plate was related to the ceramic cone. Increasing the area of the ceramic cone can effectively reduce the stress on the backplane.

(3) The influence of the structures of different ceramic panels and metal plates on the antipenetration performance was analyzed. The results indicated that increasing the thickness of ceramic optimized the antipenetration performance of the target but did not delay the ceramic breaking time. The antipenetration performance of the composite armor was the best in the sequence of Al6061/Al$_2$O$_3$/TC4/Kevlar®/TC4 when the thickness ratio of the TC4 transition and back plates is 4:3.

Acknowledgments

Nomenclature————————————————————

V_0 : Initial velocity
V_r : Residual velocity
A : Thickness ratio

References

[1] C. H. Yang et al., Analysis of the low velocity impact response of functionally graded carbon nanotubes reinforced composite spherical shells, *J. Mech. Sci. Technol.*, 32 (6) (2018) 2681-2691.

[2] J. Radin and W. Goldsmith, Normal projectile penetration and perforation of layered targets, *Int. J. Impact. Eng.*, 7 (2) (1988) 229-259.

[3] M. W. Ali et al., An experimental and numerical investigation of the ballistic response of multi-level armor against armor piercing projectiles, *Int. J. Impact Eng.*, 110 (SI) (2017) 47-56.

[4] P. K. Jena et al., An experimental study on the ballistic impact behavior of some metallic armor materials against 7.62 mm deformable projectile, *Mater. & Des.*, 31 (7) (2010) 3308-3316.

[5] M. M. Shokrieh and G. H. Javadpour, Penetration analysis of a projectile in ceramic composite armor, *Compos. Struct.*, 82 (2) (2008) 269-276.

[6] I. Marom and S. R. Bodner, Projectile perforation of multi-layered beams, *Int. J. Mech. Sci.*, 21 (8) (1979) 489-504.

[7] C. W. Ong et al., Advanced layered personnel armor, *Int. J. Impact Eng.*, 38 (5) (2011) 369-383.

[8] D. Hu et al., Investigation on the ballistic behavior of mosaic SiC/UHMWPE composite armor systems, *Ceram. Int.*, 43 (13) (2017) 10368-10376.

[9] W. L. Goh et al., Effects of hardness of steel on ceramic armor module against long rod impact, *Int. J. Impact Eng.*, 109 (2017) 419-426.

[10] Q. Wang, Z. Chen and Z. Chen, Design and characteristics of hybrid composite armor subjected to projectile impact, *Mater. Des.*, 46 (2013) 634-639.

[11] A. Kolopp, S. Rivallant and C. Bouvet, Experimental study of sandwich structures as armor against medium-velocity impacts, *Int. J. Impact Eng.*, 61 (2) (2013) 24-35.

[12] J. G. Hetherington, The optimization of two component composite armors, *Int. J. Impact Eng.*, 12 (3) (1992) 409-414.

[13] M. Lee and Y. H. Yoo, Analysis of ceramic/metal armor systems, *Int. J. Impact Eng.*, 25 (9) (2001) 819-829.

[14] R. Cortés et al., Numerical modelling of normal impact on ceramic composite armors, *Int. J. Impact Eng.*, 12 (4) (1992) 639-650.

[15] J. Z. Li, L. S. Zhang and F. L. Huang, Experiments and simulations of tungsten alloy rods penetrating into alumina ceramic/603 armor steel composite targets, *Int. J. Impact Eng.*, 3 (2017) 101: 1-8.

[16] D. Bürger et al., Ballistic impact simulation of an armor-piercing projectile on hybrid ceramic/fiber reinforced composite armors, *Int. J. Impact Eng.*, 43 (5) (2012) 63-77.

[17] J. Shi and D. Grow, Effect of double constraints on the optimization of two-component armor systems, *Compos. Struct.*, 79 (3) (2007) 445-453.

[18] C. C. Holland et al., Effect of design on the performance of steel-alumina bilayers and trilayers subject to ballistic impact, *Mech. Mater.*, 91 (2015) 241-251.

[19] J. J. Demange, V. Prakash and J. M. Pereira, Effects of material microstructure on blunt projectile penetration of a nickel-based super alloy, *Int. J. Impact Eng.*, 36 (8) (2009) 1027-1043.

[20] G. R. Johnson and W. H. Cook, Fracture characteristics of three metals subjected to various strains, strain rates, temperatures and pressures, *Eng. Fract. Mech.*, 21 (1) (1985) 31-48.

[21] D. Fernández-Fdz, R. Zaera and J. Fernández-Sáez, A constitutive equation for ceramic materials used in lightweight armors, *Comput. Struct.*, 89 (23-24) (2011) 2316-2324.

[22] X. Wang and J. Shi, Validation of Johnson-Cook plasticity and damage model using impact experiment, *Int. J. Impact Eng.*, 60 (2013) 67-75.

[23] A. Serjouei et al., Empirical ballistic limit velocity model for bi-layer ceramic-metal armor, *Int. J. Prot. Struct.*, 6 (3) (2015) 509-527.

[24] M. J. Pawar et al., Comparison of ballistic performances of Al_2O_3 and AlN ceramics, *Int. J. Impact Eng.*, 98 (2016) 42-51.

[25] A. Serjouei et al., Experimental validation of BLV model on bi-layer ceramic-metal armor, *Int. J. Impact Eng.*, 77 (2015) 30-41.

[26] T. J. Holmquist, G. R. Johnson and C. M. Lopatin, High strain rate properties and constitutive modeling of glass, *15th International Symposium on Ballistics,* Jerusalem, Israel (1995) 237-244.

[27] G. R. Johnson and T. J. Holmquist, Response of boron carbide subjected to large strains, high strain rates, and high pressures, *J. Appl. Phys.*, 85 (12) (1999) 8060-8073.

[28] T. J. Holmquist, D. W. Templeton and K. D. Bishnoi, Constitutive modeling of aluminum nitride for large strain, high-strain rate, and high-pressure applications, *Int. J. Impact Eng.*, 25 (3) (2001) 211-231.

[29] T. J. Holmquist and G. R. Johnson, Modeling prestressed ceramic and its effect on ballistic performance, *Int. J. Impact Eng.*, 31 (2) (2005) 113-127.

[30] T. J. Holmquist and G. R. Johnson, A computational constitutive model for glass subjected to large strains, high strain rates and high pressures, *J. Appl. Mech.*, 78 (5) (2011) 051003.

[31] D. C. Drucker and W. Prager, Soil mechanics and plastic analysis or limit design, *Q. Appl. Math.*, 10 (2) (1952) 157-165.

[32] A. K. Bandaru et al., Ballistic impact response of Kevlar® reinforced thermoplastic composite armors, *Int. J. Impact Eng.*, 89 (2016) 1-13.

[33] J. Sun et al., The delamination of carbon fiber reinforced composites during cutting by flexible linear shaped charge, *J. Mech. Sci. Technol.*, 34 (4) (2020) 1515-1522.

[34] B. Loret and J. H. Prevost, Dynamic strain localization in

elasto-(visco-)plastic solids, Part 1. General formulation and one-dimensional examples, *Comput. Method Appl. M,* 83 (3) (1990) 247-273.
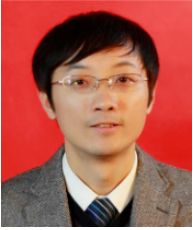
Jianzhong Lai serves as a Professor at the School of Materials Science and Engineering, Nanjing University of Science and Technology, Nanjing, China. He received his Ph.D. from Southeast University. His research interests include advanced composite and 3D printing materials.